Materials Today Bio 24 (2024) 100902

Contents lists available at ScienceDirect

Materials Today Bio

journal homepage: www.journals.elsevier.com/materials-today-bio

Tumor microenvironment responsive nano-platform for overcoming sorafenib resistance of hepatocellular carcinoma

Wenjing Xu [a,b,1], Meng Yang [d,1], Wenning Zhang [c], Weilu Jia [b], Haidong Zhang [b], Yewei Zhang [c,*]

[a] Department of Hepatobiliary and Pancreatic Surgery, The Second Affiliated Hospital, Zhejiang University School of Medicine, Hangzhou, 310009, China
[b] School of Medicine, Southeast University, Nanjing, 210009, China
[c] Department of Hepatobiliary and Pancreatic Surgery, The Second Affiliated Hospital of Nanjing Medical University, Nanjing, 210003, China
[d] Department of Ultrasound, State Key Laboratory of Complex Severe and Rare Diseases, Peking Union Medical College Hospital, Chinese Academy of Medical Sciences, Beijing, 100005, China

ARTICLE INFO

Keywords:
Tumor microenvironment response
Sorafenib resistance
Phototherapy
Multimodality imaging
Hollow MnO_2

ABSTRACT

Hepatocellular carcinoma (HCC) is a malignant tumor, which seriously jeopardizes human health. The 5-year relative survival rate of HCC is only about 18%. Sorafenib, a small molecule multi-targeted tyrosine kinase inhibitor (MTKI), has been classified as the first-line treatment scheme for HCC and has significantly extended the median survival time for patients with advanced HCC. Nevertheless, the emergence of sorafenib resistance has substantially hampered its further clinical application. Herein, the nano-platform based on phototherapy and small molecular targeted therapy (SMTT) was devised to overcome the sorafenib resistance and reduce the adverse effects. Hollow mesoporous manganese dioxide (H–MnO_2) was prepared by hard template method, and the prepared H–MnO_2 was used to load sorafenib and Chlorin e6 (Ce6). Subsequently, the nanoparticle (NPs) were modified with dopamine to optimize biocompatibility. The final prepared NPs (MCS NPs) exhibit regular spherical shape with a hydrated particle size of approximately 97.02 nm. MCS NPs can not only possess tumor microenvironment (TME) stimuli-responsive drug release performance but also can enhance the efficacy of photodynamic therapy and reverse sorafenib resistance by alleviating tumor hypoxia. Under the action of phototherapy (Ce6) combined with molecular targeted therapy (sorafenib), MCS NPs manifest a satisfactory antitumor effect for sorafenib-sensitive or sorafenib-resistant HCC cells, and retain the antiangiogenic properties of sorafenib. In the nude mouse subcutaneous tumor model constructed with sorafenib-resistant cells, MCS NPs demonstrated superior tumor imaging ability and excellent biocompatibility. The tumor inhibition rate of the MCS NPs group without laser irradiation was 53.4 %, while the MCS NPs group with laser irradiation was as high as 100 %. The novel smart TME-responsive nano-platform shows great potential for overcoming sorafenib resistance and realizes multimodality imaging and therapy of HCC.

1. Introduction

Hepatocellular carcinoma (HCC) is the most common primary liver malignancy and is ranked as the sixth most frequent cancer worldwide, with the second lowest 5-year relative survival rate [1–3]. Despite remarkable outcomes that have been achieved in the diagnosis and treatment of HCC, the survival rate of HCC patients has not been effectively improved [4]. High mortality of HCC is mainly attributed to the lack of effective therapeutic measures. The traditional therapeutic tactics, such as surgery, radiotherapy, and chemotherapy, exist various defects [5]. For instance, the surgical indication for HCC is narrow, and surgical resection is mainly suitable for patients with single tumors and liver function in the compensatory period [6]. In addition, HCC is not sensitive to radiation and chemotherapy due to its own biological characteristics, which affects the effectiveness of transformation therapy. Radiotherapy and chemotherapy can also damage the human immune system, causing cancer cells to lose immune monitoring and accelerate proliferation [7]. Although liver transplantation has a good therapeutic effect on HCC patients with multiple liver tumors and decompensated liver function. However, the lack of available organs suitable for patients limits the widespread application of liver transplantation [5]. These defects bringing great dilemma to the therapy of

* Corresponding author.
E-mail address: zhangyewei@njmu.edu.cn (Y. Zhang).
[1] These authors contributed equally to this work.

https://doi.org/10.1016/j.mtbio.2023.100902
Received 8 July 2023; Received in revised form 26 November 2023; Accepted 3 December 2023
Available online 15 December 2023

HCC.

In recent years, small molecule multi-targeted kinase inhibitors (MTKI) have presented inspiring therapeutical effects owing to the advantages of superior targeting performance and satisfactory tolerance [8,9]. As a typical MTKI, sorafenib has been recommended as an effective therapeutic pharmaceutical for advanced HCC by the U.S. Food and Drug Administration (FDA) [10,11]. Sorafenib can inhibit tumorous proliferation and angiogenesis, by targeting multiple serine/threonine kinases, including *c*-RAF, transmembrane platelet-derived growth factor receptor beta (PDGFRB), and vascular endothelial growth factor receptors (VEGFR1, VEGFR2, VEGFR3), etc [12]. Two vital phases III clinical trials have demonstrated obvious survival improvement for patients with advanced HCC treated with sorafenib [13]. Although sorafenib displayed desirable anticancer efficacy for HCC, numerous serious hurdles appear in the course of clinical therapy, bringing substantial roadblocks to the treatment of HCC. Firstly, the low bioavailability of sorafenib oral tablets limited its potential application, resulting from its poor solubility in water (approximately 1.7 μg/mL) and rapid metabolism [14]. Secondly, the dose of sorafenib in clinical applications commonly needs to be strictly controlled due to its serious side effects including skin toxicity, diarrhea and hypertension, and so on [15]. Thirdly, the response rate of sorafenib is low, with only 30 % of patients can benefit from sorafenib treatment [16]. Fourthly, the most underlying issue to underscore is that sorafenib often encounters clinical treatment failure because of drug resistance [17]. Typically, sorafenib resistance is susceptible to occur within six months of treatment. The mutation and activation of the parallel signaling pathway, such as abnormal signal activation of AKT, and the mutation of VEGFR, are likely to cause sorafenib resistance during the treatment of HCC [17–19]. Moreover, previous studies have shown that hypoxia is also one of the possible mechanisms for sorafenib resistance [20,21]. Hypoxia can upregulate HIF-1α expression, which can activate MDR1 gene, increase the expression of *P*-gp encoded by MDR1, and then reduce the intracellular concentration of chemotherapy drugs, including sorafenib. Therefore, downregulating HIF-1α expression by implementing an anti HIF strategy, has become ideal to overcome sorafenib resistance [22]. The past years have witnessed that quite a few nanoplatforms were designed to avoid the occurrence of drug resistance, enhance biocompatibility, and improve therapeutical efficiency [23–27]. Among these studies, phototherapy including photodynamic therapy (PDT) and photothermal therapy (PTT) has drawn substantial attention on account of high selectivity, relative noninvasiveness, and no resistance compared with traditional therapeutic modalities [28–31]. The nano-drug delivery system could effectively kill tumor cells and simultaneously inhibit tumor angiogenesis by the synergistic effort of phototherapy and small molecule targeted therapy (SMTT) [32,33]. Whereas, the tumor blood vessel disruption cuts off nutrient and oxygen (O_2) supply for tumor tissue, realizing tumor hunger treatment, and exacerbating hypoxia status [32]. Despite spatiotemporal features for targeted cancer should be considered in the combination with anti-angiogenic therapy and PDT, the aggravating hypoxia may severely impede the therapeutic efficiency of PDT after a period of anti-angiogenic treatment [33,34]. Consequently, it is indispensable for us to discover innovative therapeutic strategies to solve this problem. As we already know, the tumor microenvironment (TME) is generally characterized by vascular abnormalities, a mildly acidic environment (pH 6.5–6.9), hypoxia, overproduced endogenous hydrogen peroxide (H_2O_2), and high glutathione (GSH) concentration, which may lead to tumor invasion, metastasis, and drug resistance [35,36]. As a typical TME-responsive nanocarrier, MnO_2 inherently can catalyze H_2O_2 to generate O_2, which can relieve hypoxia and potentiate the effect of PDT [37–40]. Under mildly acidic, MnO_2 is degraded to water-soluble Mn^{2+} which is a perfect magnetic resonance image (MRI) contrast agent and simultaneously consumes reduced GSH to oxidized glutathione (GSSG) [41–43]. Besides, nanostructured MnO_2 has the inherent features of excellent biocompatibility and satisfactory loading capacity, which avoid long-term toxicity in vivo [44]. Based on the above factors, MnO_2 had attracted extensive attention as a TME-responsive multifunctional agent for improving the efficiency of tumor therapy [38,45].

Herein, focused on the difficulties and deficiencies in the clinical application of sorafenib, hollow mesoporous MnO_2 NPs (H–MnO_2) were synthesized as a carrier of sorafenib and photosensitizer (Ce6). After superficial modification with polydopamine (PDA), the final NPs (MCS NPs) were prepared and composed of H–MnO_2, sorafenib, Ce6, and PDA (Scheme 1a). The hollow mesoporous structure of H–MnO_2 improves the drug loading rate, and the introduction of PDA addresses the issues of poor water solubility and premature release of the loaded drugs [46,47]. The MCS NPs achieve drug response release peculiarity owing to the depolymerization of PDA and degradation of H–MnO_2 in TME. Meanwhile, the MCS NPs with a nano-size of about 97 nm tumors can selectively accumulate in the tumor site via the enhanced permeability and retention (EPR) effect, which holds great promise for multimodal imaging, including fluorescent images, photothermal images, and MRI. Under illumination by 660 nm laser, abundantly produced O_2 and continuously released Ce6 boost antitumor efficiency of PDT (Scheme 1b). Both in vitro and in vivo studies confirmed that the PDT/PTT/SMTT synergistic therapeutic method was potent to overcome sorafenib resistance and enhance anti-tumor efficiency.

2. Results and discussion

2.1. Synthesis and characterization of H–MnO_2 NPs

The transmission electron microscope (TEM) image of $sSiO_2$ showed a regular spherical shape, and the hydrated particle size was about 65.85 ± 1.36 nm (Fig. 1a and d). After the shell of MnO_2 is coated, a thin layer structure can be observed on the surface (Fig. 1b). As shown in Fig. 1c, the TEM image of H–MnO_2 presented spherical morphology and hollow structure, and the particle size of H–MnO_2 increases to 73.31 ± 4.12 nm (Fig. 1e). The Zeta potentials of $sSiO_2$, $sSiO_2$@MnO_2, and H–MnO_2 are −50.53 ± 0.47 mV, −38.67 ± 1.49 mV, and −37.87 ± 0.76 mV, respectively (Fig. 1f). No significant changes were observed for the hydrated particle size of MCS NPs over 14 days, indicating MCS NPs has good stability (Figure S2). As shown in the X-ray photoelectron spectroscopy (XPS) spectrum (Fig. 1g), the characteristic peaks at 642.5 eV and 653.9 eV correspond to the Mn $2_{p2/3}$ and Mn $2_{p1/2}$ spin-orbital peaks of MnO_2, which means the +4 valence state of Mn in NPs [44,48,49]. As illustrated in Fig. 1h and i, the surface area and average pore diameter of H–MnO_2 were measured to be 276 $m^2\ g^{-1}$ and 4 nm, respectively, by Brunauer-Emmett-Teller (BET). The high specific surface area proves its hollow structure, and the non-overlapping nitrogen adsorption and desorption curves, as well as the average pore size of 4 nm, indicates that the mesoporous structure of H–MnO_2. The H–MnO_2 with mesoporous property and large surface area is expected to be a suitable nanosystem to load photosensitizers and small molecule targeted drugs for synergistic therapy of tumor.

2.2. Synthesis and characterization of MCS NPs

The prepared H–MnO_2 was applied for the delivery of sorafenib and Ce6, and the surface of H–MnO_2 was modified with PDA to enhance biocompatibility. The MCS NPs revealed spherical hollow morphology from the TEM image (Fig. 2a) and presented a relatively homogeneous size of about 97.02 ± 5.89 nm (Fig. 2b), which demonstrated a suitable size for the EPR effect. The average polydispersity index (PDI) of the MCS NPs was 0.21 ± 0.05, and photos of the MCS NPs showcased no obvious precipitation (Fig. 2b), which proved that MCS NPs have remarkable dispersion peculiarity and stability. The UV–vis absorption spectrum manifests that MCS NPs have an obvious absorbance band with characteristic absorption peaks of sorafenib at 275 nm, and Ce6 at 418 nm and 677 nm, respectively, indicating successful encapsulation of sorafenib and Ce6. MCS NPs also showed a 14 nm red-shift compared to

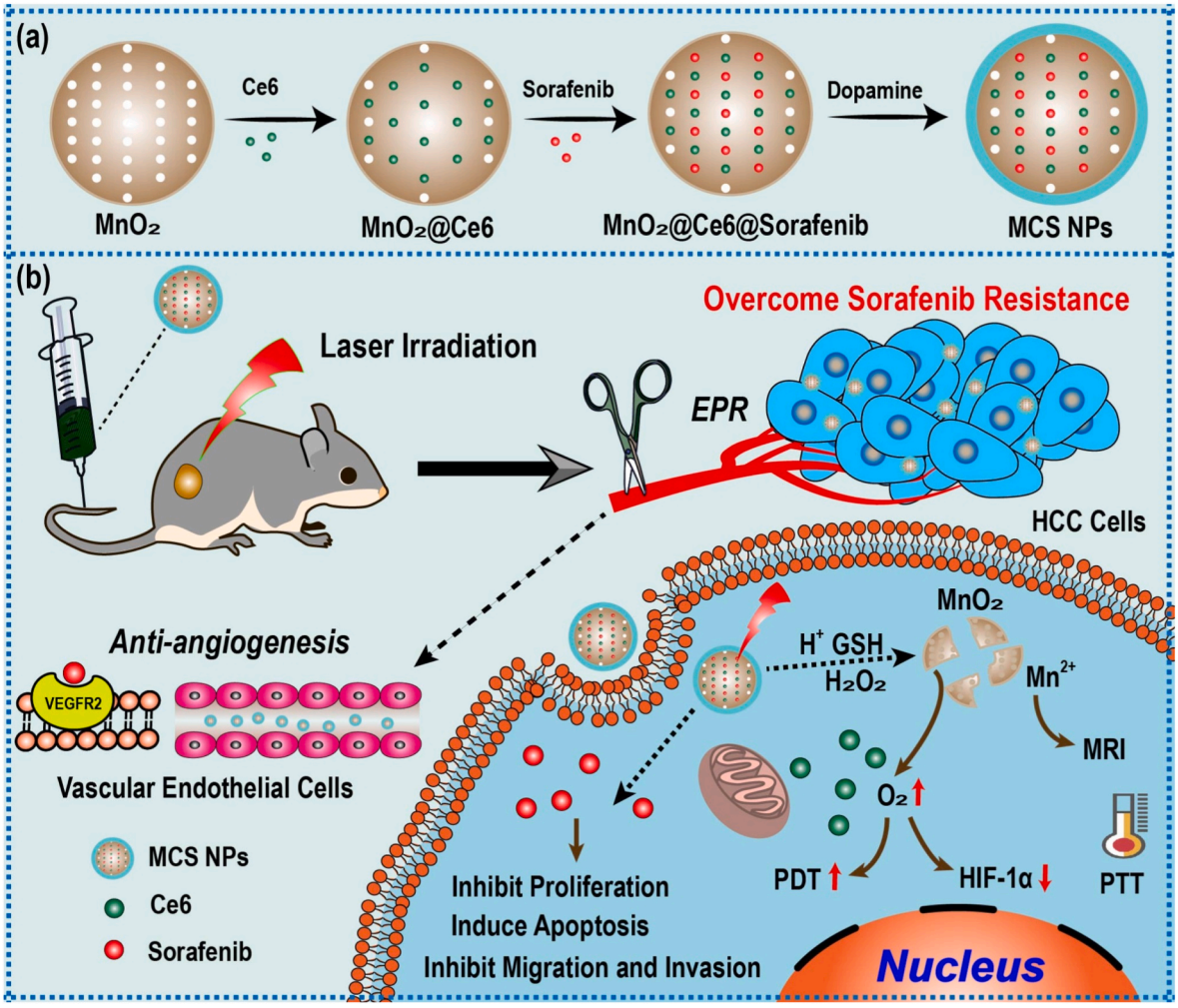

Scheme 1. (a) Schematic illustration of the fabrication of MCS NPs. (b) Anticancer schematic illustration of TME-responsive MCS NPs.

the absorption peak (663 nm) of Ce6 (Fig. 2c). The encapsulation efficiency of sorafenib and Ce6 were 71.63 ± 1.74 % and 93.12 ± 2.35 %, respectively. The drug loading efficiency of sorafenib and Ce6 were 14.67 ± 0.36 % and 19.11 ± 0.48 %, respectively. There is a report that indicates the loading rate of Ce6 increases with the feeding weight ratio (Ce6: H–MnO_2) the mass ratio of Ce6 to H–MnO_2 [38]. We choose the feeding weight ratio (Ce6 and sorafenib: H–MnO_2) is balance the drug loading efficiency and the enhanced PDT effect of Ce6 by O_2 from H–MnO_2.

It is well known that the characteristics of TME include hypoxia, high GSH concentration (2–10 μM), an acidic microenvironment (pH 6.5–6.9), high levels of H_2O_2 in tumors (50–100 μM), vascular abnormalities, and so on [50,51]. An excellent TEM stimulus-responsive carrier should be able to degrade smoothly in the TEM.

$$MnO_2 + 2GSH + 2H^+ \rightarrow Mn^{2+} + GSSG + 2H_2O \quad (1)$$

$$MnO_2 + H_2O_2 + 2H^+ \rightarrow Mn^{2+} + 2H_2O + O_2 \quad (2)$$

As described in Equation (1), H–MnO_2 was decomposed accompanied by degradation of GSH, demonstrating H–MnO_2 possesses superior GSH-response release ability. Furthermore, MnO_2 can react with H_2O_2 in an acidic environment to produce O_2 (Equation (2)). To explore the depleting performance of H–MnO_2 to GSH, the UV–vis absorption of 5,5′-Dithiobis-(2-nitrobenzoic acid) (DTNB) with 1 mM GSH and H–MnO_2 was measured. The result showed an obvious GSH depleting capacity of H–MnO_2 (Figure S3). To verify the O_2-producing ability of prepared MCS NPs, the MCS NPs were dispersed in an H_2O_2 aqueous solution (100 μM) at pH 6.5 (mimicking the TME), and subsequently dissolved O_2 levels were tested over time. The experiment results showed that the MCS NPs could effectively decompose H_2O_2 to release O_2 at pH 6.5 with H_2O_2 compared with the neutral environment (pH 7.4) (Fig. 2d). Noteworthily, the generation efficiency of dissolved O_2 was influenced by a H–MnO_2 concentration-dependent manner. As H–MnO_2 is degraded, its concentration gradually decreases, which lead to that the generation efficiency of O_2 also gradually decreases [38]. It is crucial whether the loaded theranostic agents can be smoothly released from the carrier. To investigate the sorafenib release capability from MCS NPs, the UV–vis spectra change of MCS NPs in the neutral environment (pH 7.4, without H_2O_2) and simulating TME (pH 6.5, 100 μM H_2O_2). As illustrated in Fig. 2e, the release rate (58.24 %) of sorafenib at pH 6.5 after 24 h incubation with H_2O_2 is higher than the release rate (19.19 %) at pH 7.4 without H_2O_2, suggesting a sustained release from the MCS NPs under acidic conditions with H_2O_2. The drug release experiment further proved the TME responsive release capacity of MCS NPs. As indicated in Fig. 2f, the decomposition of H–MnO_2 was measured by UV absorption spectroscopy. The result displayed that the absorbance of MnO_2 appeared to be stable under pH 7.4 with the degradation rate of MnO_2 less than 20 % after 6 h, while the degradation rate exceed 80 % under pH 6.5 in the presence of H_2O_2 (100 μM) at 37 °C, further demonstrating the TME-responsive degradation performance of H–MnO_2. The generation of reactive oxygen species (ROS), in particular singlet oxygen ($^1O_2$), is crucial for the PDT effect of the photosensitizer. The hypoxia status of solid tumors severely hampers the therapeutic efficacy of PDT, especially type II PDT. To evaluate the PDT efficiency of

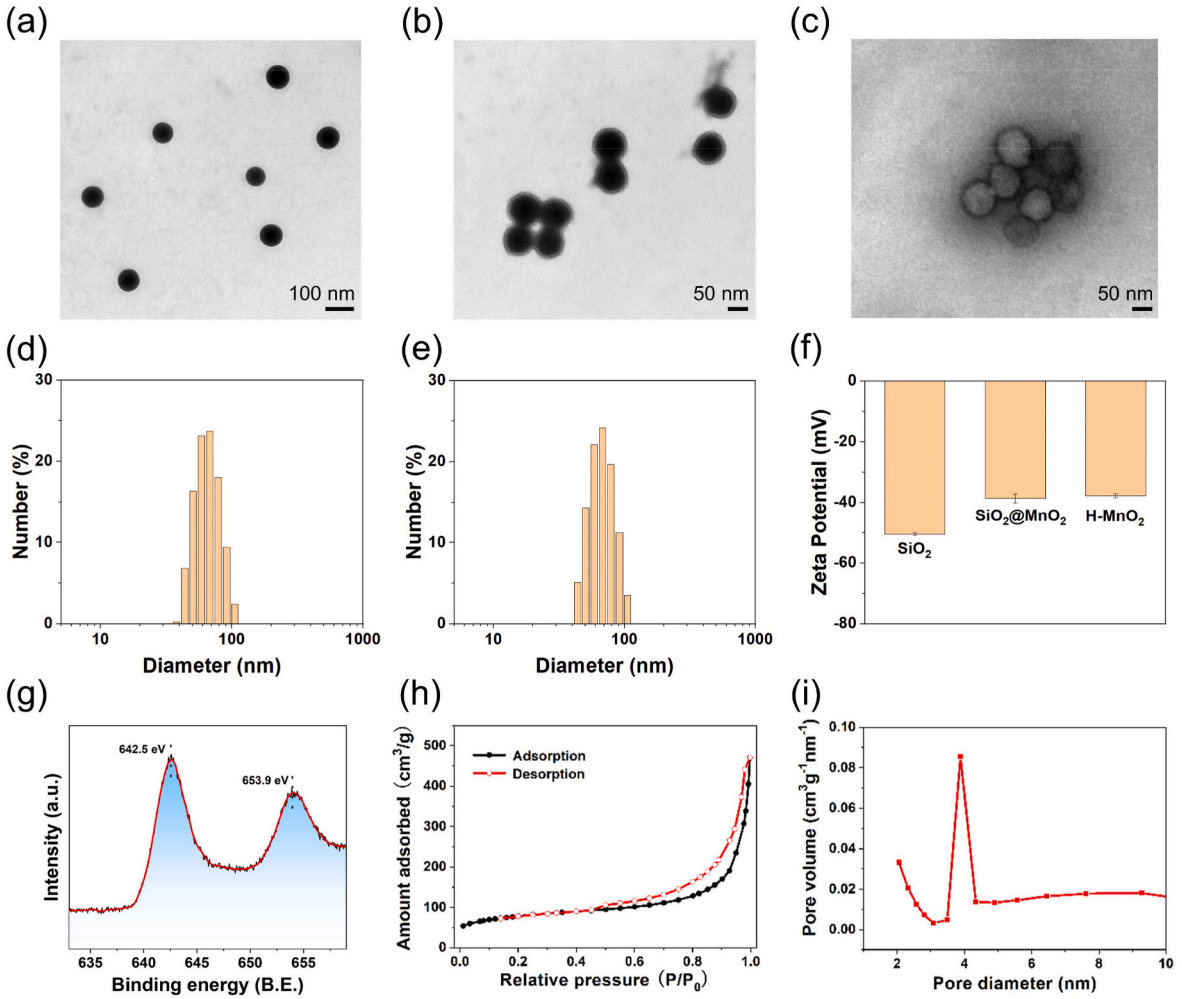

Fig. 1. (a, b) TEM images of $sSiO_2$, $sSiO_2$@MnO_2, and H–MnO_2 NPs. (d, e) The DLS size distribution of $sSiO_2$ and H–MnO_2 NPs in water, respectively. (f) Zeta potential of $sSiO_2$, $sSiO_2$@MnO_2, and H–MnO_2 NPs. (n = 3, mean ± SD). (g) XPS spectrum of H–MnO_2 NPs. (h) N_2 adsorption/desorption isotherms of the H–MnO_2. (i) The pore-size distribution curve of the H–MnO_2.

MCS NPs, we studied whether the produced O_2 by MCS NPs facilitated the generation of $^1O_2$ in vitro. Singlet oxygen sensor green (SOSG) as the $^1O_2$ indicator and H_2O_2 was added to the aqueous dispersion of MCS NPs and Ce6. As demonstrated in Fig. 2g–i and Figure S4a-c, the fluorescence enhancement of SOSG by MCS NPs with H_2O_2 is higher than Ce6 with or without H_2O_2, and MCS NPs without H_2O_2, further indicating that the additional O_2 supply by H–MnO_2 activated $^1O_2$ generation. In addition, PTT is also an important pattern of phototherapy. To interrogate the photothermal effect of MCS NPs, the temperature change of MCS NPs aqueous solutions was recorded by an IR thermal camera under 660 nm laser irradiation for 12 min. As shown in Fig. 2j, with the increase of laser power, the temperature change caused by MCS NPs (50 μg/mL) increased gradually. Similarly, the concentration of MCS NPs also affected the efficiency of PTT. The MCS NPs (100 μg/mL) can lead to a temperature change of more than 20 °C under 660 nm laser irradiation (500 mW/cm^2), which provides a theoretical basis for PTT and photothermal imaging (Fig. 2k). The photothermal effect may originate from the successful loading of Ce6 and the photothermal effect of PDA and MnO_2 [32,52,53]. MCS NPs also displayed good photothermal cycling stability which is a crucial characteristic for PTT. The MCS NPs (75 μg/mL) were irradiated by 660 nm laser (500 mW/cm^2) for five ON-OFF cycles, and the maximum temperature change of MCS NPs remained nearly constant (Fig. 2l). In conclusion, the above experiment results indicated that the MCS NPs can realize TME response release and O_2-self-generating synergistic PDT/PTT therapy.

2.3. Evaluation of therapeutic efficacy for sorafenib-sensitive cells in vitro

It is of importance for oncotherapy whether the NPs could be endocytosed by tumor cells. As shown in Fig. 3a, the red fluorescence images observed with the laser confocal microscope indicated the MCS NPs were abundantly dispersed in the cytoplasm after endocytosis, suggesting that MCS NPs exhibit superior uptake ability in Hep3B, SMMC7721, and SMMC7721/S HCC cells. Additionally, the green fluorescence proved that the tumor cells that endocytosed NPs can produce substantial endogenous ROS after 660 nm laser radiation. Before the biomedical application of any nanomaterials, the biotoxicity of the nanocarrier is imperative to be estimated. MTT (3-(4,5-dimethylthiazol-2-yl)-2,5-diphenyltetrazolium bromide) assay was performed to detect the cytotoxicity of H–MnO_2-PDA to sorafenib-sensitive HCC cell lines (Hep3B and SMMC7721) and sorafenib-resistant HCC cell lines (SMMC7721/S) in vitro. The cytotoxicity of H–MnO_2-PDA exerts extremely weak at the concentration range of 10–100 μg/mL. The cell viability was more than 80 % even at a high concentration (100 μg/mL), indicating the satisfactory biosecurity of H–MnO_2-PDA with (Figure S5) or without 660 nm laser radiation (Fig. 3b). Whereafter, we further verified the therapeutic effects of different treatment groups on Hep3B cells. The Ce6 group showed negligible dark toxicity for Hep3B cells, while the cell viability of MCS NPs group and sorafenib group dramatically declined with sorafenib dose dependence in darkness (Figure S6). After 660 nm laser irradiation, the cell viability of the MCS NPs group

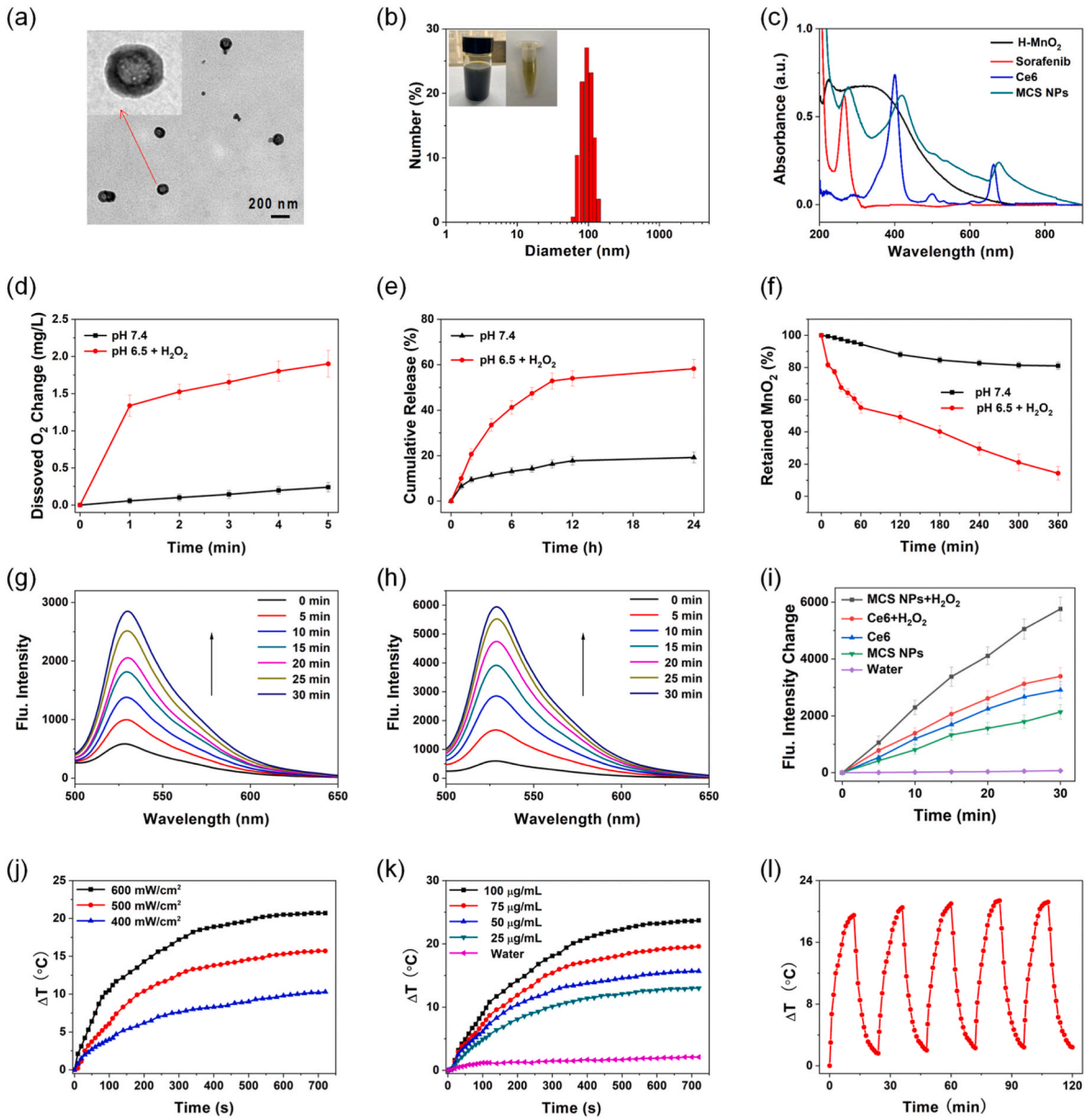

Fig. 2. (a) TEM images of MCS NPs. The inset showed the magnified TEM images. (b) The DLS size distribution of MCS NPs in water. The inset showed the photos of MCS NPs. (c) Absorption spectra of H–MnO_2, sorafenib, Ce6, and MCS NPs. (d) O_2 production of MCS NPs dispersed with pH 7.4 in water and pH 6.5 in H_2O_2 solutions (100 μM), n = 3, mean ± SD. (e) The release rate of sorafenib from MCS NPs at pH 7.4 in water and pH 6.5 in H_2O_2 solutions (100 μM), n = 3, mean ± SD. (f) The degradation of H–MnO_2 by measuring the absorbance spectra. n = 3, mean ± SD. (g, h) Fluorescence spectra (529 nm) of SOSG (10 μM) mixed with Ce6 without H_2O_2 and MCS NPs with H_2O_2 solutions, respectively. (i) Fluorescence intensity increases curves of SOSG from (g, h). (j, k) The temperature change of MCS NPs at different power and concentrations under 660 nm laser (500 mW/cm^2), respectively. (l) Photothermal heating and cooling cycles of MCS NPs aqueous solution (75 μg/mL) with laser radiation (500 mW/cm^2).

was particularly lower than that of the Ce6 group (Figure S7). In Fig. 3c, the MCS NPs group with 660 nm laser irradiation also showed the most effective SMMC7721 cell-killing ability than other groups. 2′,7′-dichlorofluorescein diacetate (DCFH-DA, a kind of ROS probe) was applied to further interrogate the ROS intracellular generation capability in vitro. As shown in Fig. 3d, the green fluorescence observed by fluorescence microscopy appears in the cytoplasm after 660 nm laser illumination at a power density of 100 mW/cm^2 for 3 min, confirming the obvious ROS generation. Compared to other groups, the MCS NPs group with light illumination exhibited the strongest green fluorescence intensity in the cytoplasm, indicating the promotion of ROS generation to enhance the efficiency of PDT. This phenomenon may be attributed to the MnO_2-triggered O_2 concentration rise stimulated by the TME. It is worth noting that the sorafenib group also showed fluorescence enhancement effect, which may be due to that sorafenib can target electron transfer chain complexes, leading to the increase of ROS generation [54,55]. Mitochondrial Membrane Potential Assy Kit (JC-1) was used to detect the mitochondrial membrane potential (MMP) change of SMMC7721 cells. When the MMP is high, JC-1 aggregates were formed in the matrix of the mitochondria, which can produce red fluorescence, while MMP is low, JC-1 cannot aggregate in the matrix of mitochondria, and green fluorescence was observed. The decrease of MMP is a hallmark event in the early stage of apoptosis. As displayed in Fig. 3e, the sample incubated with the MCS NPs group under 660 nm lasers emitted strong green fluorescence than other groups, indicating that mitochondrial dysfunction could be induced by MCS NPs. It is noteworthy that the sorafenib group and the MCS NPs group could also cause the decrease of MMP, which may be due to the fact that sorafenib, as an MTKI, could

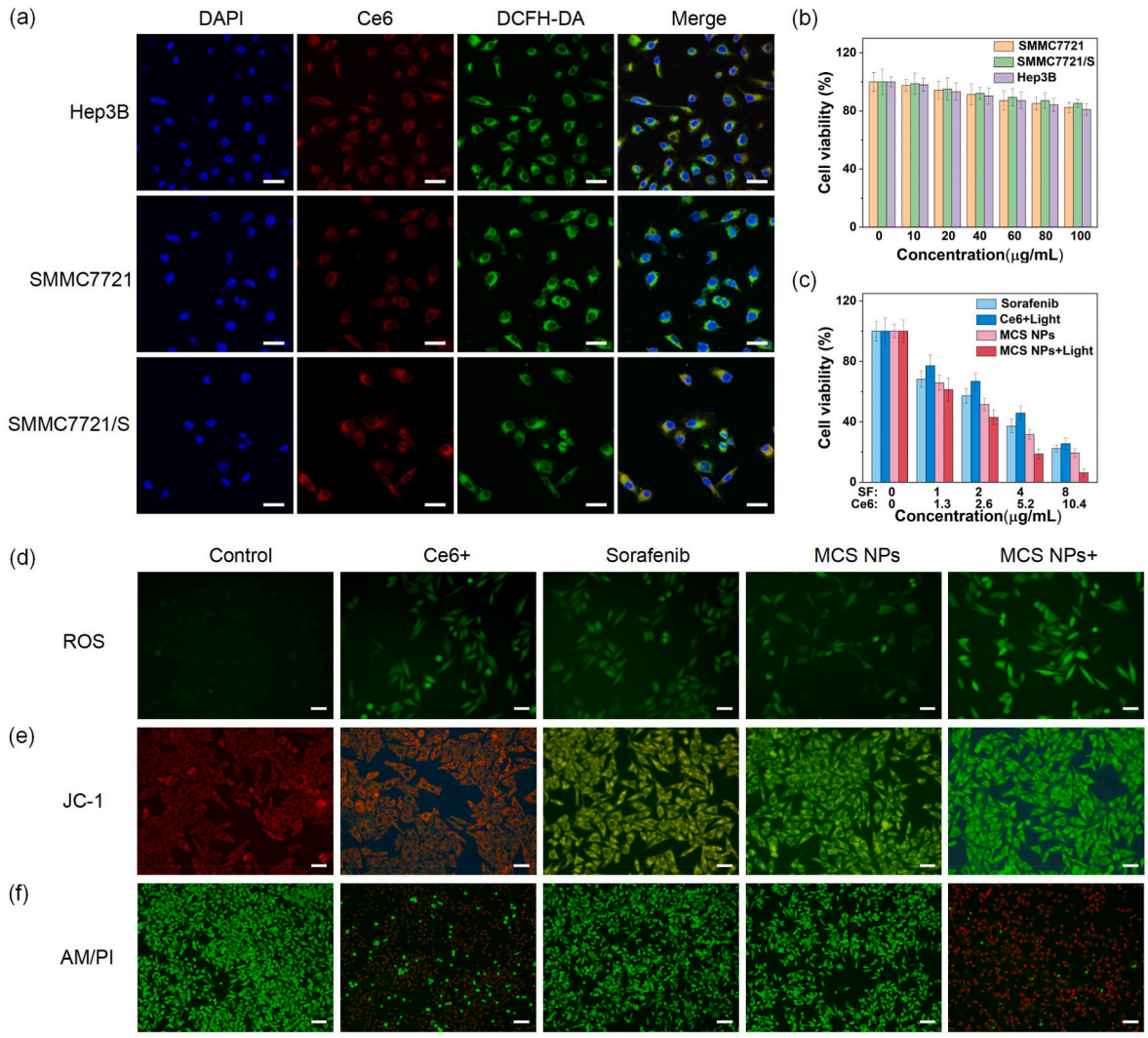

Fig. 3. (a) Confocal fluorescence images of Hep3B, SMMC7721, and SMMC7721/S cells. Scale bar: 30 μm. DAPI (Ex = 405 nm), Ce6 (Ex = 633 nm), DCFH-DA (Ex = 488 nm). (b) Viabilities of Hep3B, SMMC7721, and SMMC7721/S cells incubated with H–MnO_2-PDA. (n = 4, mean ± SD). (c) Relative cell viability of SMMC7721 incubated with sorafenib, Ce6 with 660 nm laser irradiation, MCS NPs, and MCS NPs with 660 nm laser irradiation (500 mW/cm^2, 3 min), (n = 4, mean ± SD). (d) SMMC7721 cells were stained by DCFH-DA after different treatments. (Control: no drugs added during the cultivation process, Ce6+: Ce6 with laser irradiation, Sorafenib: sorafenib without laser irradiation, MCS NPs: MCS NPs without laser irradiation, MCS NPs+: MCS NPs with laser irradiation). Scale bar: 50 μm. (e) JC-1 staining of SMMC7721 cells to explore changes for mitochondrial membrane potential in different groups. Scale bar: 50 μm. (f) Living/dead double staining for SMMC7721 cells treated with various groups. Scale bar: 100 μm. Ce6 (4.37 μg/mL), sorafenib (3.36 μg/mL), MCS NPs (Ce6: 4.37 μg/mL, sorafenib: 3.36 μg/mL).

reduce MMP by inhibiting the oxidative respiratory chain and activating multiple pathways such as Bax and Caspase-3 [56]. Subsequently, the combined therapeutic effect was also investigated by calcein (AM) and propidium iodide (PI) which can stain live and dead cells, respectively. Phototherapy was performed after 12 h with the various treatments, and the tumor cells of the Ce6 group and MCS NPs group exposed to the laser were killed quickly. Strikingly, the red fluorescence in MCS NPs with 660 nm laser irradiation is more visually obvious than in other groups (control, free sorafenib, Ce6 with light, and MCS NPs without light), indicating the remarkable synergetic therapeutic effects based on phototherapy and SMTT (Fig. 3f).

2.4. Overcome sorafenib resistance in vitro

The problem of sorafenib resistance has always restricted its widespread application. We used sorafenib-resistant HCC cell lines (SMMC7721/S) to further evaluate the therapeutic efficacy of MCS NPs. As exhibited in Fig. 4a, the half-maximal inhibitory concentration (IC50) of sorafenib for SMMC7721 was 2.53 μg/mL, while the IC50 for SMMC7721/S was 18.42 μg/mL. The SMMC7721/S tumor cell lines demonstrated strong resistance to sorafenib, which seriously restricted the clinical efficacy of sorafenib. In Fig. 4b, the prepared MCS NPs with 660 nm laser radiation presented the strongest therapeutic efficiency than other groups (sorafenib, Ce6 + light, and MCS NPs), which proved that the permutation combinatorial therapeutical tactic based on sorafenib and phototherapy is a fascinating avenue to overcome sorafenib resistance. In addition, the MCS NPs group without laser illumination displayed lower cell viability than the free sorafenib group, and the possible reason includes, (1) the increased drug absorption rate, (2) the reconstructed TME by H–MnO_2 (the improved hypoxia, the decreased GSH concentration, etc) reversed sorafenib resistance and increased sensitivity of drug-resistant cells to sorafenib [21,22]. The flow cytometry apoptosis experiment further proved the excellent effect of MCS NPs in overcoming drug resistance. The MCS NPs with light irradiation can significantly promote cell apoptosis, SMMC7721/S cells experienced 51.9 % late apoptosis and 18.7 % early apoptosis when the sorafenib concentration is 4.05 μg/mL (Fig. 4c). Quantitative analysis result further confirmed that the apoptosis rate of MCS NPs with light

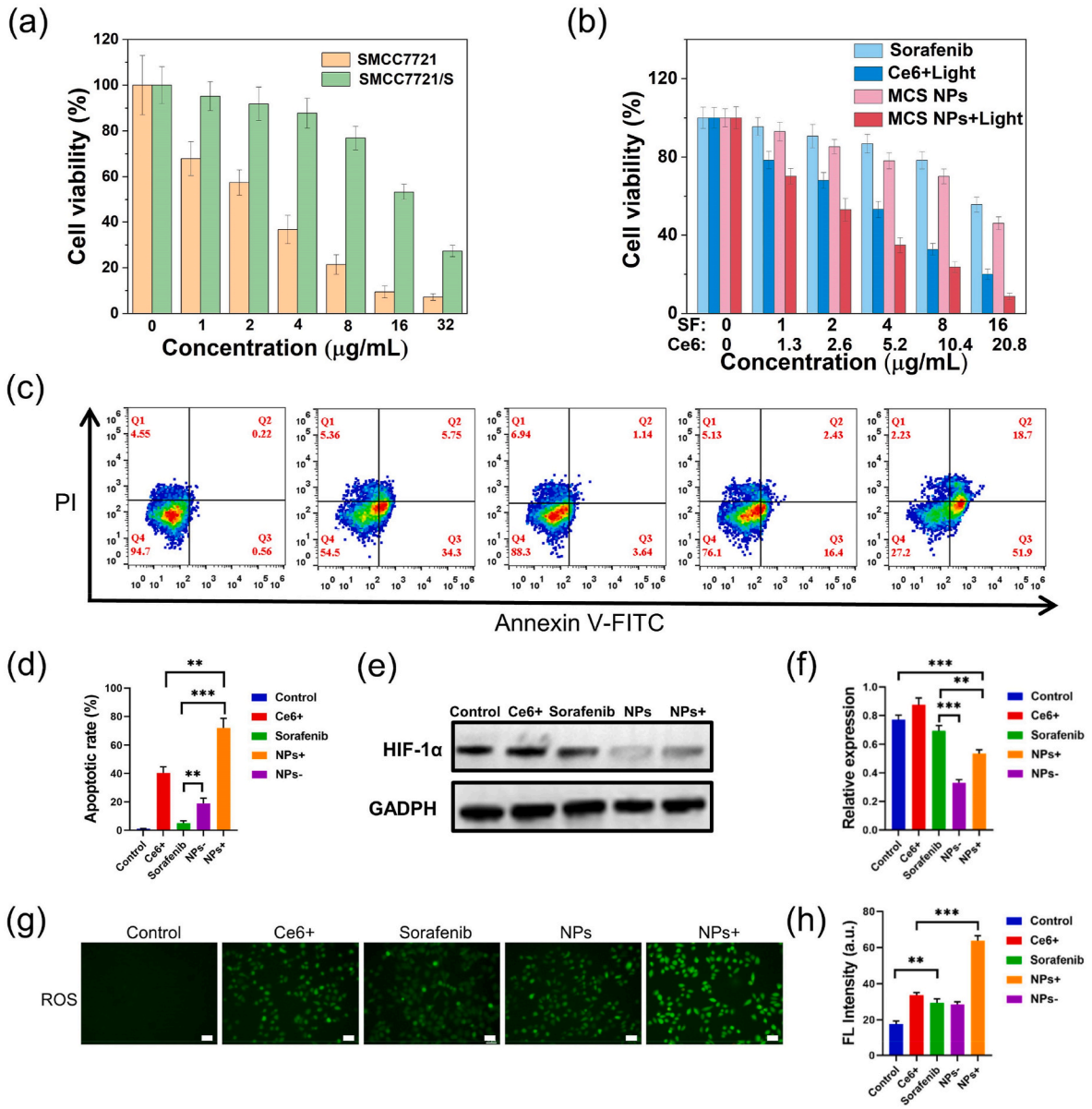

Fig. 4. (a) Cell viability experiment of SMMC7721 and SMMC7721/S cells incubated by various concentrations of sorafenib. (n = 4, mean ± SD). (b) Relative cell viability of different treatments for SMMC7721/S cells. (n = 4, mean ± SD). (c, d) Flow cytometric analysis on the apoptosis levels of SMMC7721/S cells after different treatments (Control, Ce6 + laser, sorafenib, MCS NPs, and MCS NPs + laser). (n = 3, mean ± SD). (Control: no drugs added during the cultivation process, Ce6+: Ce6 with 660 nm laser irradiation, Sorafenib: sorafenib without laser irradiation, NPs: MCS NPs without laser irradiation, NPs+: MCS NPs with laser irradiation). (e, f) Western blotting showed the HIF-1α expression levels after treatment with Ce6 + laser, sorafenib, MCS NPs, and MCS NPs + laser for 24 h (n = 3, mean ± SD). (g) ROS generation of SMMC7721/S cells. Scale bar: 50 μm. (h) Quantitative fluorescence intensity of ROS by different treatments. (n = 3, mean ± SD). **P < 0.01, ***P < 0.001, *t*-test. Ce6 (5.26 μg/mL), sorafenib (4.05 μg/mL), MCS NPs (Ce6: 5.26 μg/mL, sorafenib: 4.05 μg/mL).

irradiation was significantly higher than that of other groups, and the apoptosis rate of MCS NPs without light irradiation was also higher than that of sorafenib group (Fig. 4d). These results were basically consistent with the results of MTT. Sorafenib resistance has been reported to be associated with genetic heterogeneity, abnormal activation of STAT3, autophagy, epithelial-mesenchymal transition, tumor microenvironment, epigenetic regulation, tumor stem cell, and so on [57]. As an important characteristic of TME, the hypoxic state causes HCC cells to be extremely resistant to sorafenib, which may be due to the increased adaptive response of HCC cells to hypoxia. In addition, hypoxia leads to the increased expression of HIF-1α. The overexpressed HIF-1α can activate the multidrug resistance gene 1 (MDR1), increase the expression of *P*-gp protein encoded by MDR1, thereby reducing the intracellular concentration of sorafenib [58]. Therefore, down-regulation of HIF-1α protein expression has emerged as a strategy to overcome HCC sorafenib resistance [59]. It is reported that the expression level of HIF-1α of sorafenib-resistant HCC cell lines incubated with sorafenib remained stable under the state of hypoxia [60]. Fig. 4e and f shows that both MCS NPs with or without laser irradiation group can significantly down-regulate the expression of HIF-1α, which is mainly attributed to the produced O_2 by H–MnO_2 effectively alleviating hypoxia. Moreover, in the process of phototherapy, the hypoxic improvement effect is stronger than the O_2 consumption of photosensitizers. The improvement of hypoxia not only enhances the efficiency of PDT but also can reverse sorafenib resistance [61,62]. The strongest green fluorescence appears in SMMC7721/S tumor cells incubated with MCS NPs after laser radiation compared to other groups, indicating the promotion of endogenous ROS generation (Fig. 4g and h, S8). This phenomenon may be

responsible for the catalytic production of O_2 from H_2O_2 by H–MnO_2. The experimental results of intracellular ROS detection were comparable to that of sorafenib-sensitive tumor cells (SMMC7721). In the JC-1 assay, after the light irradiation, the SMMC7721/S tumor cells incubated with MCS NPs cause the most significant changes in MMP, indicating the synergistic therapy based on phototherapy and SMTT could severely interfere with mitochondrial function (Figure S9). Subsequently, the effect of MCS NPs on the migration and invasiveness of SMMC7721 was evaluated. As shown in Figure S10, the transwell experiments proved that MCS NPs can effectively inhibit the invasion and migration of SMMC7721/S. MCS NPs with laser irradiation can effectively inhibit the proliferation, migration, and invasion of SMMC7721/S cells and promote cell apoptosis by reducing the expression level of HIF-1α, promoting ROS production, and reducing mitochondrial membrane potential. All in all, the prepared MCS NPs with or without irradiation can more robustly kill sorafenib-resistant and sorafenib-sensitive cells than free sorafenib treatment in vitro. The MCS NPs can overcome sorafenib resistance by integrating the PDT/PTT/SMTT synergistic effect.

2.5. Anti-angiogenesis assay in vitro

As an important part of SMTT, the anti-angiogenic effect of sorafenib is an effective strategy to inhibit the growth of tumors. As shown in Fig. 5a, MCS NPs can effectively killing HUVEC cells in vitro, and the IC50 of MCS NPs for HUVEC cells was 9.21 μg/mL. The MCS NPs can be successfully endocytosed by HUVEC cells (Fig. 5b). Then, a flow cytometry assay was further used to examine the antitumor efficacy of MCS NPs. As shown in Fig. 5c, MCS NPs (9.21 μg/mL) in dark can promote HUVEC cell apoptosis as well as free sorafenib, with 25.6 % late-stage apoptosis and 14.9 % early-stage apoptosis, which further confirmed that NPs can effectively kill vascular endothelial cells. To further evaluate the anti-angiogenic action of MCS NPs, the vessel formation and disruption assay was performed. Both MCS NPs and free sorafenib could destroy the tubes from HUVECs on matrigel via anti-angiogenesis, in comparison, no significant vascular damage was observed in the blank group (Fig. 5d). Besides, similar to free sorafenib, MCS NPs also showed a superior ability to inhibit the migration of HUVEC cells (Fig. 5e and f). The expression of VEGFR2 in HUVEC was significantly reduced after treatment with sorafenib and MCS NPs, indicating that MCS NPs can inhibit angiogenesis by target VEGFR2 (Fig. 5g). Indeed, the above results indicate that the MCS NPs exhibit similar antiangiogenic activity as free sorafenib, which indicated that the anti-vascular properties of sorafenib were not affected by the nano-assembled MCS NPs. Consequently, MCS NPs can also play the same anti-vascular effect as free sorafenib.

2.6. Multi-modal imaging in vivo

The imaging detection of HCC is of great significance for early diagnosis of HCC, intraoperative localization, determination of surgical margins, and so on. Among them, real-time fluorescence imaging plays a pivotal role in the fluorescence calibration of the surgical target area and in assisting the surgeon to perform precise surgical operations. The MCS NPs were injected into SMMC7721/S tumor-bearing mice through the tail vein. As shown in Fig. 6a, there was no fluorescence appeared before the injection of the MCS NPs solution. However, after 2 h post-injection of MCS NPs, it was observed that the fluorescence signal exhibited gradual accumulation in the tumor site, suggesting MCS NPs start to enter the tumor tissues. With MCS NPs gradually accumulated in the tumor site, the fluorescence signal reached the maximum at about 8 h, indicating that MCS NPs have a significant targeted feature to the tumor tissues by the EPR effect. The quantitative analysis of fluorescence intensity further demonstrates this phenomenon (Fig. 6b). The Ex vivo fluorescence images of the tumor and main organ tissues further manifest the remarkable targeting performance of MCS NPs (Fig. 6c, S11).

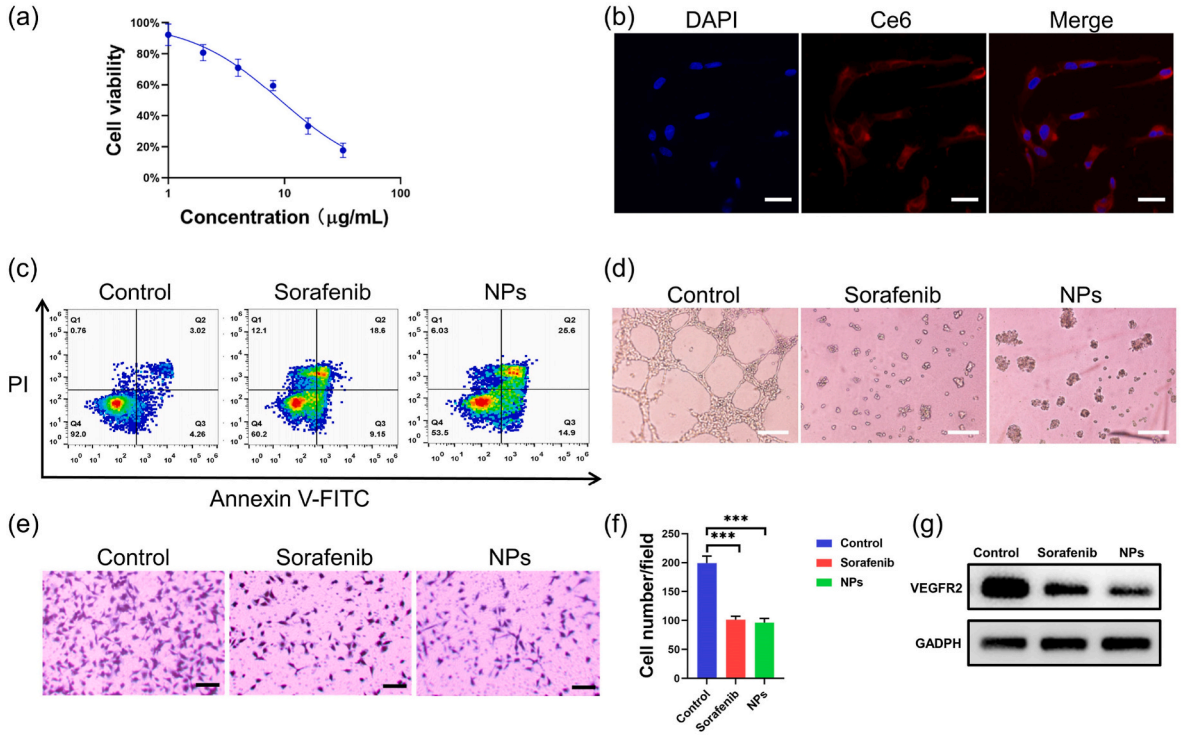

Fig. 5. (a) Cell viability of HUVEC cells incubated with different concentrations MCS NPs without laser irradiation. (n = 4, mean ± SD). (b) Confocal fluorescence images of HUVEC cells. Scale bar: 30 μm. DAPI (Ex = 405 nm), Ce6 (Ex = 633 nm). (c) Flow cytometric analysis on the apoptosis levels of HUVEC cells treated with sorafenib and MCS NPs. (d) Effect of sorafenib and MCS NPs on HUVECs tube formation incubated with listed reagents for 8 h. Scale bar: 100 μm. (e) Cell migration experiment of HUVEC after various treatments, including the control group, sorafenib group, and MCS NPs group. Scale bar: 100 μm. (f) Quantitative analysis of the number of cell migration in different groups. (g) The expression of VEGFR2 protein in HUVEC cells under different treatment conditions.

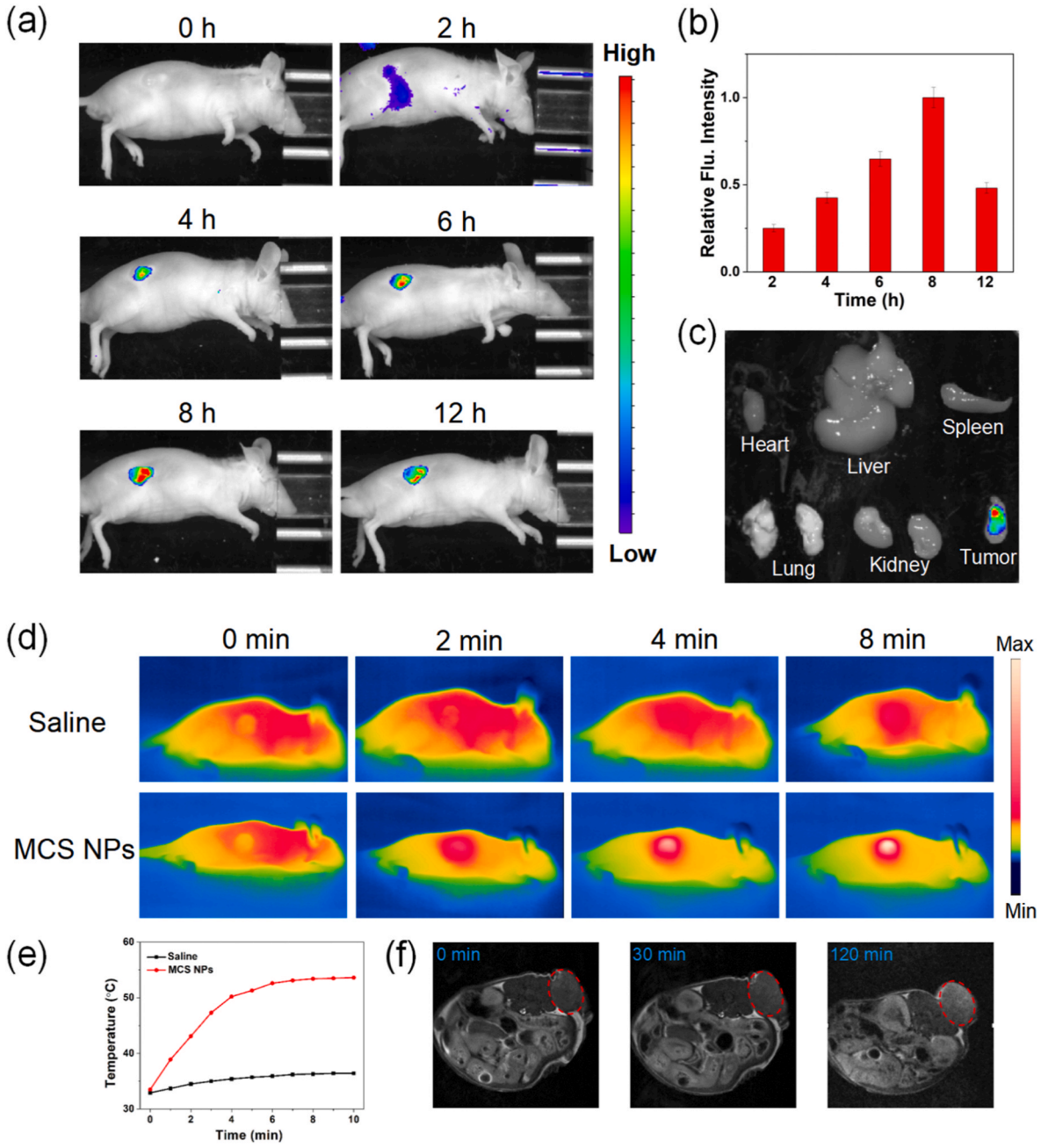

Fig. 6. (a) In vivo real-time and in vivo fluorescence imaging of SMMC7721/S tumor-bearing mice with intravenous injection of MCS NPs. (b) Fluorescence intensity changes in tumor tissues at different time points (n = 3, mean ± SD). (c) Ex vivo fluorescence images of the tumor and main organ tissues dissected from mice at 12 h. (d) Thermal imaging of tumor-bearing mice injected with saline or MCS NPs under 660 nm laser irradiation for different times. Saline: inject with physiological saline, MCS NPs: inject with MCS NPs. (e) Heating curves. (f) In vivo T2-weighted MRI of SMMC7721/S tumor-bearing mouse models.

Real-time photothermal imaging plays an important role in PTT. As shown in Fig. 6d and e, the temperature monitored by IR thermal camera reached a plateau from 33.5 °C to 53.6 °C in tumor regions, while that of the control group with saline injection shows little change. It can be concluded that MCS NPs possess the excellent ability of photothermal conversion for photothermal imaging. In the actual clinical application, although the penetration depth of the laser is restrained, MCS NPs may show application value in intraoperative illumination localization and dissection of residual tumor tissue. Previous studies have proved that H–MnO_2 could augment T1 and T2 signals of magnetic resonance (MR) in vivo imaging due to the generation of Mn^{2+}. As considered an ideal substitute for gadolinium (conventional MRI contrasting agent), MnO_2 has superior biocompatibility. Interestingly, the unique hollow structure also showed elevated water permeability which further improved r1 and r2 values (the essential parameters for MRI) [63]. As shown in Fig. 6f and Figure S12, the MRI exhibited that the tumor area had higher MR signal intensity treated with MCS NPs for 120 min post-injection. In a word, multi-modal imaging based on various imaging technologies can be achieved by the EPR effect of MCS NPs, which will be beneficial to the precise diagnosis and intraoperative navigation treatment of HCC.

2.7. *In vivo antitumor efficacy*

It would be highly desirable to evaluate the biocompatibility of MCS NPs, which will affect transport in the blood. The hemolytic toxicity of MCS NPs was detected and the result demonstrated that the red blood

cells (RBCs) remained intact (hemolysis ratio less than 5 %), after incubating with various concentrations of MCS NPs for 6 h, which proved the biosecurity of MCS NPs for intravenous injection (Fig. 7a). Inspired by the TME-responsive release ability of MCS NPs, the synergistic therapeutic efficacy of MCS NPs was further evaluated systematically with SMMC7721/S tumor-bearing nude mice in vivo. When the tumor sizes reached about 75 mm^3, the tumor-bearing nude mice were randomly divided into five groups for treatment: (i) saline solution injection without any irradiation, (ii) free sorafenib injection without any irradiation, (iii) MCS NPs dispersion injection without any irradiation, (iv) free Ce6 dispersion injection with 660 nm laser irradiation, and (v) MCS NPs dispersion injection with 660 nm laser irradiation. Subsequently, nude mice were intravenously injected with the therapeutic agent, and the tumor sites were exposed to 660 nm laser irradiation for 15 min at 8 h post-injection. Fig. 7b and d shows the average tumor volume changes during the 14 days of treatment. The volume of tumors in the control group increased quickly, and the group injected with sorafenib and Ce6 under 660 nm laser illumination showed minor tumor suppression, while the group injected with MCS NPs exhibited a noticeable suppressive effect. This phenomenon may be attributed to (1) the successful intratumoral accumulation of MCS NPs through the EPR effect, and (2) the changes of TME increase sensitivity to sorafenib. Furthermore, the group injected with MCS NPs under 660 nm laser illumination can eliminate the tumor and show no tumor recurrence, which may be caused by the outstanding synergistic PDT/PTT/SMTT therapeutic outcome of MCS NPs. During this treatment, no abnormalities were found in the body weight of mice in each group (Fig. 7c). Pathologically, as displayed in Fig. 7e, the hematoxylin and eosin (H&E) staining of tumor slices image of MCS NPs with laser illumination exhibited a large area of necrosis or apoptosis after two treatments,

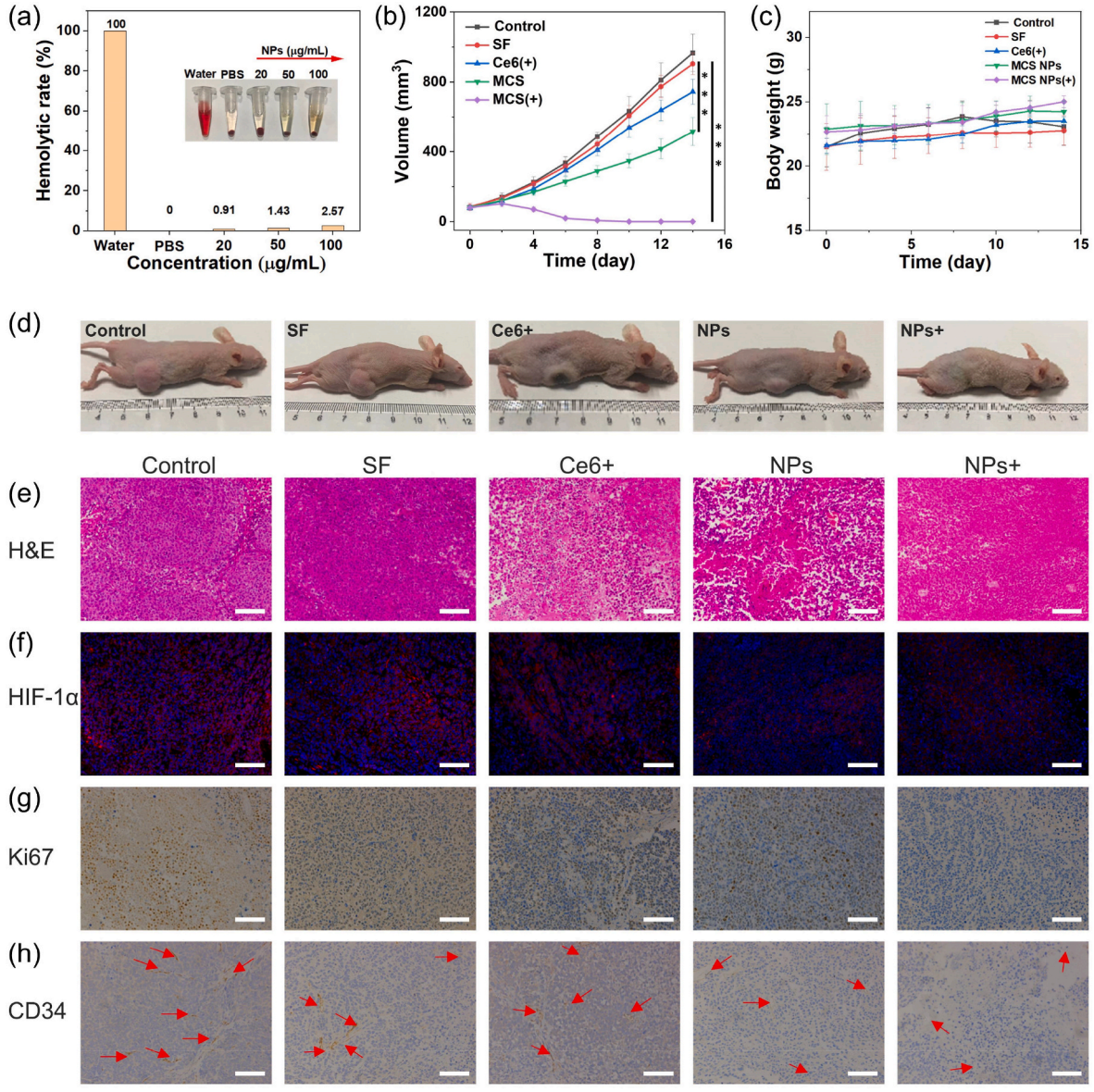

Fig. 7. (a) Hemolysis of MCS NPs at various concentrations. (b) The time-dependent volume of SMMC7721/S tumor-bearing mice after systemic administration of different treatments. (SF: sorafenib) (n = 5, mean ± SD, ***P < 0.001, *t*-test). (c) Body weight changes of tumor-bearing mice during treatment. (n = 5, mean ± SD). (d) Photographs of five group tumor-bearing after treatment. (e) The H&E-stained tumor slices were photographed in different groups after two treatments. Scale bar: 100 μm. (f) The fluorescence images of SMMC7721/S tumor slices were collected from different groups. The nuclei and hypoxic areas were stained with DAPI (blue), and HIF-1α antibody (red), respectively. Scale bar: 100 μm. (g) The Ki67-stained tumor slices were collected from mice for different groups after two treatments. Scale bar: 100 μm. (h) Blood vessel staining (CD34) of tumor tissue after different treatments. The red arrows indicate capillaries. Scale bar: 100 μm. (For interpretation of the references to color in this figure legend, the reader is referred to the Web version of this article.)

confirming the remarkable therapeutic effect of MCS NPs. Additionally, immunofluorescence staining of HIF-1α was performed to investigate the tumor O_2 generation capability of the MCS NPs. The tumor tissue was stained with DAPI (blue) and *anti*–HIF–1α antibodies (red). The considerably reduced HIF-1α expression injected with MCS NPs after laser irradiation indicates that the MCS NPs can relieve tumor hypoxia (Fig. 7f). The Ki67 staining was employed to assess the proliferative capacity of various groups. In the group of MCS NPs, the brown area was dramatically reduced compared to the other groups, which elucidated the remarkable anti-proliferative ability of MCS NPs (Fig. 7g). Previously, we evaluated the antiangiogenic ability of MCS NPs in vitro. The CD34 (a specific marker of vascular endothelium) staining was performed to further verify the anti-vascular ability in vivo. As shown in Fig. 7h, vessel damage could be observed in the group treatment of MCS NPs with or without laser irradiation, further indicating the significant anti-angiogenic effect of MCS NPs. It is well known that Ce6 exhaust O_2 during the progress of type II PDT, combined with the anti-vascular effect of sorafenib will aggravate hypoxia. Whereas, the MCS NPs with laser illumination showed slightly improved hypoxia compared to the control group. The reasons may be the continuous O_2 production by H–MnO_2 and the promoting effect of photothermal on blood flow. In addition, the anti-angiogenic effect in vivo needs a period of treatment to play its role, and phototherapy can directly kill tumor tissue after illuminating the tumor site enriched with MCS NPs. This spatiotemporal specificity can enable MCS NPs to promote phototherapy and overcome sorafenib resistance by relieving hypoxia in the early stage, and cooperate with anti-vascular therapy to achieve tumor starvation treatment in the late stage, further killing tumor tissue.

2.8. *In vivo biocompatibility of MCS NPs*

As shown in Fig. 8a, the blood routine analysis, including red blood cells (RBC), white blood cells (WBC), platelets (PLT), hemoglobin (HGB), hematocrit (HCT), mean corpuscular volume (MCV), and mean corpuscular hemoglobin concentration (MCHC), were measured on 7 and 14 days. No abnormal change could be found for mice injected with MCS NPs in 14 days, and all indicators are within the normal reference range, indicating the superior biosafety of the MCS NPs. Furthermore, the pathological slice of the major organs (heart, liver, spleen, lung, and kidney) was stained by H&E. Compared with the control group, no significant damage and necrosis of the major organs was observed after 14 days of treatment, further confirming that MCS NPs possess superior biocompatibility (Fig. 8b). In addition, we also investigated the pharmacokinetics of MCS NPs in vivo. After intravenous injection of MCS NPs (300 μL, 500 μg/mL), 10uL of blood was collected from the ocular plexus of mice at certain time intervals, and the amount of Mn in the blood was measured by ICP-MS. As shown in Figure S13, the diffusion and elimination half-live of MCS in the bloodstream were calculated to be 0.50 h and 4.33 h, respectively. Long blood circulation time is beneficial for passive targeting of tumors through the EPR effect. Meanwhile, MCS NPs can be effectively cleared after a period of time, further indicating its biological safety. Taken together, MCS NPs is a suitable TME response nanoplatform for multi-modal cancer therapy.

3. Conclusions

In summary, activatable TME-responsive nanoplatforms based on H–MnO_2 were developed for the co-delivery of sorafenib and Ce6. H–MnO_2 in MCS NPs can react with endogenous H_2O_2 and H^+ in TME to produce O_2. The generated O_2 can relieve the hypoxic condition and maximize the therapeutic potential of PDT after 660 nm laser irradiation. Meanwhile, hypoxia improvement may reverse sorafenib resistance via downregulating the expression of HIF-1α. MCS NPs showed superior biocompatibility and can directly kill tumor cells or inhibit tumors by cutting off tumor blood vessels. The multifunctional MCS NPs showed superior antitumor efficiency for both sorafenib-sensitive HCC cell lines (Hep3B and SMMC7721) and sorafenib resistance HCC cell lines (SMMC7721/S). In the sorafenib-resistant mouse subcutaneous tumor model, MCS NPs can enrich the tumor site through the EPR effect. Concurrently, the H–MnO_2 shell was decomposed to produce Mn^{2+} and realize the TME-responsive release of sorafenib and Ce6. The generated Mn^{2+} can be applied for MRI, while the released Ce6 can be used for fluorescence and photothermal imaging. The multi-modal imaging can realize an early accurate diagnosis and intraoperative navigation of HCC. Meanwhile, the remarkable PDT/PTT/SMTT synergistic therapeutic efficiency of the versatile nano-platform provides an unprecedented idea for overcoming sorafenib resistance.

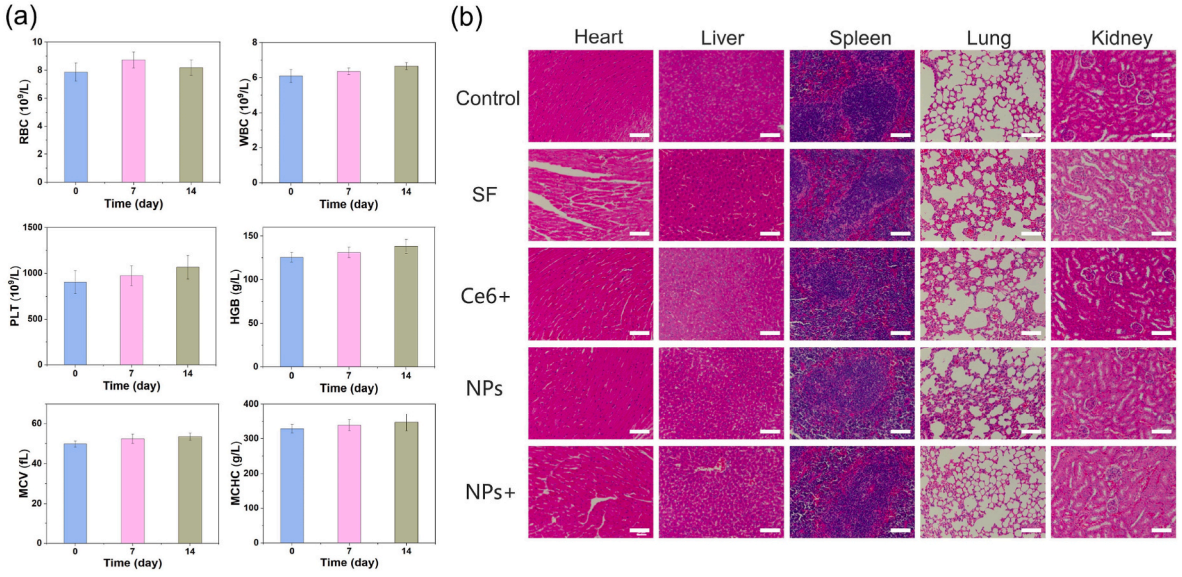

Fig. 8. (a) Blood routine tests for WBC, RBC, PLT, HGB, MCV, and MCHC in 14 days. (n = 3, mean ± SD). (b) The H&E stained images of heart, liver, spleen, lung, and kidney slices from mice for different groups after 14 days of treatment. Scale bar: 100 μm.

4. Experimental section

4.1. Preparation of hollow mesoporous MnO_2 and MCS NPs

Firstly, monodispersed silica NPs were synthesized, as follows: 37 mL ethanol, 5 mL in deionized water, and 1.57 mL ammonia solution were mixed in an oil bath at 50 °C for 10 min. Then, 2 mL of tetraethyl orthosilicate (TEOS) was added dropwise. The mixture was stirred in an oil bath (600 r/min, 50 °C) for 4 h. The obtained solid silica NPs ($sSiO_2$ NPs) were washed three times with ethanol and dissolved in 20 mL of deionized water. Subsequently, 1 g potassium permanganate ($KMnO_4$) was dispersed in 20 mL of deionized water. The $KMnO_4$ solution was added dropwise into the aqueous solution of $sSiO_2$ NPs with sonication. The above mixture was ultrasonicated for 4 h and then stirred at room temperature for 24 h (600 r/min). The product ($sSiO_2$@MnO_2) was repeatedly centrifuged (11,000 r/min, 10 min) and washed three times with deionized water. Finally, the H–MnO_2 was obtained after dissolving the silica template with 2 M sodium bicarbonate (Na_2CO_3) solution for 12 h 10 mg H–MnO_2 was dispersed into 5 mL of deionized water. 10 mg sorafenib and 10 mg Ce6 were dissolved in 5 mL of ethanol [32,64]. The mixed solution (sorafenib and Ce6) was added to 5 mL H–MnO_2 solution. Subsequently, the solution was shocked by ultrasound and dialysis. The obtained solution was centrifuged for 10 min (11,000 r/min). The prepared H–MnO_2 was dispersed in 10 mL of Tris buffer (pH 8.5) containing dopamine hydrochloride (10 mg). The above solution was stirred at room temperature for 24 h (600 r/min). The final NPs (MCS NPs) was obtained after centrifugation and washing.

4.2. Singlet oxygen detection of MCS NPs

The singlet oxygen generation of MCS NPs (50 μg/mL) in the presence or absence of H_2O_2 (100 μM) was detected with SOSG (10 μM) as a singlet oxygen fluorescent probe. The mixture of MCS NPs and SOSG was illuminated under 660 nm laser (100 mW/cm^2) for 30 min, and the fluorescence intensity of SOSG was measured under a 480 nm excitation.

4.3. Photothermal properties of MCS NPs

1 mL of MCS NPs aqueous solution (0, 25, 50, 75, and 100 μg/mL) was irradiated with 660 nm laser. The temperature data was recorded by a laser temperature camera.

4.4. Photostability

MCS NPs went through 5 cycles of temperature rise and decrease to validate the photostability (75 μg/mL, 500 mW/cm^2).

4.5. Cell culture

Hep3B, SMMC7721, SMMC7721/S, and HUVEC cells were obtained from Southeast University. Hep3B was cultured in a DMEM medium containing fetal bovine serum (FBS, 10 %) and antibiotics (1 %) at 37 °C and 5 % CO_2 atmosphere. The SMMC7721 and SMMC7721/S were cultured in a 1640 medium containing fetal bovine serum (FBS, 10 %) and antibiotics (1 %) at 37 °C and 5 % CO_2 atmosphere. HUVECs were cultured in HUVEC specific medium at 37 °C and 5 % CO_2 atmosphere.

4.6. Cytotoxicity assay

The tumor cell lines were seeded in 96-well plates and were cultivated in DMEM or 1640 medium containing various concentrations of MCS NPs. The cells were incubated in dark for 12 h and then irradiated with a 660 nm laser (3 min, 500 mW/cm^2). After another 12 h of incubation, 50 μL of MTT (5 mg/mL) was added to each well and incubated for another 4 h. MTT assays were conducted to determine the cell viability. The absorption at 570 nm was measured by a microplate analyzer.

4.7. Confocal fluorescence imaging of cellular uptake

In the cellular uptake examination, Hep 3B cells, SMMC7721, SMMC7721/S, and HUVEC cells were dealt with MCS NPs (2 μg/mL) for 12 h in glass bottom petri dishes. Subsequently, these cells were irradiated with a 660 nm laser (3 min, 100 mW/cm^2). The cells were stained with DCFH-DA (10 μM) and 4′,6-diamidino-2-phenylindole DAPI (15 μM). After incubation in the incubator for 30 min, these samples were observed with Olympus FV3000 confocal fluorescence microscope.

4.8. Detection of ROS generation in vitro

DCFH-DA (10 μM) was used to detect the ROS in cells. After 12 h of incubation of MCS NPs, the light group was irradiated with a 660 nm laser for 3 min at a power density of 100 mW/cm^2. Subsequently, DCFH-DA was used for staining tumor cells. After incubation for 30 min, an inverted fluorescence microscope was used to collect images.

4.9. Detection of mitochondrial membrane potential

Tumor cells were incubated in culture dishes for 12 h. Samples were irradiated with a 660 nm laser. After being washed with PBS, the cells were stained with JC-1 solution for 25 min. Subsequently, the mitochondrial membrane potential was immediately detected by a fluorescence microscope.

4.10. Animals and tumor model

Male athymic nude mice (5 weeks old, about 20 g, permit number: SYXK (Su) 2016–0014) were bought from Changzhou Cavens Laboratory Animal corporation. The procedures were approved by Southeast University. The mice were subcutaneously inoculated with SMMC7721/S cells (100 μL, 2×10^6 cells) in the right back. Saline, free Ce6 (6.5 mg/kg), free sorafenib (5 mg/kg), and MCS NPs (sorafenib dose: 5 mg/kg) were injected into nude mice through the tail vein. After 8 h, the tumor sites were irradiated with 660 nm light at a power density of 500 mW/cm^2 for 15 min. After irradiation, tumor volumes of mice have recorded with the following formula: volume = width × length × height × 0.52. The treatments were performed by one time every two days. The sizes of tumors were recorded to monitor the tumor growth every two days, and mice were sacrificed by cervical dislocation after 14 days.

4.11. Hemolysis assay

The RBCs were obtained from athymic nude mice and were stored in the test tube containing heparin saline solution (1000 U/mL). 1 mL of a solution containing 4 % erythrocyte and MCS NPs of varying concentrations (10, 25, 50, 100 μg/mL) were incubated at 37 °C for 6 h. Then the sample was centrifuged at 8000 rpm, the supernatants were collected and the absorption of the supernatant was measured at 540 nm. The percentage of hemolysis was calculated by the following formula: hemolysis% = $(A_{sample} - A_{PBS})/(A_{water} - A_{PBS}) \times 100$ % (A_{water}, A_{PBS} refer to the absorption at 540 nm of water and PBS).

4.12. In vivo imaging

In vivo fluorescence imaging was performed using Fluor Vivo 2000 INDEC Biosystem. SMMC7721/S tumor-bearing mice were injected with 200 μL MCS NPs (sorafenib dose: 5 mg/kg, Ce6 dose: 6.5 mg/kg). Images were taken by the fluorescence-imaging instrument at 0, 2, 4, 6, 8, and 12 h post-injection.

4.13. MIR

The mice were anesthetized by chloral hydrate. After intravenous injection of MCS NPs, mice were scanned at different time points by the Bruker BioSpec 94/30 USR MR scanner (Bruker, Germany).

4.14. Histology Sample preparation

After two treatments, a nude mouse was randomly selected, and tumor tissue was taken for histopathology analysis by H&E, HIF-1α, Ki67, and CD34 staining assays. The others nude mice were sacrificed (after treatment for 14 days) to obtain organs (heart, liver, spleen, lung, and kidney). Organs were separated and fixed with 4 % para-formaldehyde for histological analysis.

CRediT authorship contribution statement

Wenjing Xu: Conceptualization, Data curation, Investigation, Methodology. **Meng Yang:** Methodology, Project administration, Software. **Wenning Zhang:** Supervision, Visualization. **Weilu Jia:** Data curation. **Haidong Zhang:** Resources, Writing - original draft. **Yewei Zhang:** Conceptualization, Funding acquisition, Validation, Writing - review & editing.

Declaration of competing interest

The authors declare that they have no known competing financial interests or personal relationships that could have appeared to influence the work reported in this paper.

Data availability

Data will be made available on request.

Acknowledgments

The work was funded by the National Natural Science Foundation of China (62331016, 62141109, 62227803), Jiangsu Province Social Development Preface Clinical Project (BE2022812), Jiangsu Province Leading Technology Basic Research Project (BK20212012).

Appendix A. Supplementary data

Supplementary data to this article can be found online at https://doi.org/10.1016/j.mtbio.2023.100902.

References

[1] L.A. Torre, F. Bray, R.L. Siegel, J. Ferlay, J. Lortet-Tieulent, A. Jemal, Global cancer statistics, Ca - Cancer J. Clin. 65 (2) (2012) 87–108, 2015.
[2] J. Bruix, G.J. Gores, V. Mazzaferro, Hepatocellular carcinoma: clinical frontiers and perspectives, Gut 63 (5) (2014) 844–855.
[3] A. Forner, M. Reig, J. Bruix, Hepatocellular carcinoma, Lancet 391 (10127) (2018) 1301–1314.
[4] R.L. Siegel, K.D. Miller, A. Jemal, Cancer statistics, Ca - Cancer J. Clin. 70 (1) (2020) 7–30, 2020.
[5] A.G. Singal, P. Lampertico, P. Nahon, Epidemiology and surveillance for hepatocellular carcinoma: new trends, J. Hepatol. 72 (2) (2020) 250–261.
[6] A. Vogel, T. Meyer, G. Sapisochin, R. Salem, A. Saborowski, Hepatocellular carcinoma, Lancet 400 (10360) (2022) 1345–1362.
[7] H.B. El–Serag, K.L. Rudolph, Hepatocellular carcinoma: epidemiology and molecular carcinogenesis, Gastroenterology 132 (7) (2007) 2557–2576.
[8] W. Xu, C. Ye, X. Qing, S. Liu, X. Lv, W. Wang, X. Dong, Y. Zhang, Multi-target tyrosine kinase inhibitor nanoparticle delivery systems for cancer therapy, Mater. Today Bio. 16 (2022), 100358.
[9] L. Huang, S. Jiang, Y. Shi, Tyrosine kinase inhibitors for solid tumors in the past 20 years (2001-2020), J. Hematol. Oncol. 13 (1) (2020) 143.
[10] A.L. Cheng, Y.K. Kang, Z. Chen, C.J. Tsao, S. Qin, J.S. Kim, R. Luo, J. Feng, S. Ye, T. S. Yang, J. Xu, Y. Sun, H. Liang, J. Liu, J. Wang, W.Y. Tak, H. Pan, K. Burock, J. Zou, D. Voliotis, Z. Guan, Efficacy and safety of sorafenib in patients in the Asia-Pacific region with advanced hepatocellular carcinoma: a phase III randomised, double-blind, placebo-controlled trial, Lancet Oncol. 10 (1) (2009) 25–34.
[11] J.K. Heimbach, L.M. Kulik, R.S. Finn, C.B. Sirlin, M.M. Abecassis, L.R. Roberts, A. X. Zhu, M.H. Murad, J.A. Marrero, AASLD guidelines for the treatment of hepatocellular carcinoma, Hepatology 67 (1) (2018) 358–380.
[12] G.M. Keating, A. Santoro, Sorafenib: a review of its use in advanced hepatocellular carcinoma, Drugs 69 (2) (2009) 223–240.
[13] S.A. Antoniu, UPLIFT Study: the effects of long-term therapy with inhaled tiotropium in chronic obstructive pulmonary disease. Evaluation of: tashkin DP, Celli B, Senn S et al.: a 4-year trial of tiotropium in chronic obstructive pulmonary disease, N. Engl. J. Med. 359 (15) (2008) 1543–1554. Expert Opin Pharmacother 10(4) (2009) 719-22.
[14] T. Zhou, X. Liang, P. Wang, Y. Hu, Y. Qi, Y. Jin, Y. Du, C. Fang, J. Tian, A hepatocellular carcinoma targeting nanostrategy with hypoxia-ameliorating and photothermal abilities that, combined with immunotherapy, inhibits metastasis and recurrence, ACS Nano 14 (10) (2020) 12679–12696.
[15] G.W. Jean, R.M. Mani, A. Jaffry, S.A. Khan, Toxic effects of sorafenib in patients with differentiated thyroid carcinoma compared with other cancers, JAMA Oncol. 2 (4) (2016) 529–534.
[16] X. Tian, T. Yan, F. Liu, Q. Liu, J. Zhao, H. Xiong, S. Jiang, Link of sorafenib resistance with the tumor microenvironment in hepatocellular carcinoma: mechanistic insights, Front. Pharmacol. 13 (2022), 991052.
[17] F. Fornari, C. Giovannini, F. Piscaglia, L. Gramantieri, Elucidating the molecular basis of sorafenib resistance in HCC: current findings and future directions, J. Hepatocell. Carcinoma 8 (2021) 741–757.
[18] T.B. Toh, J.J. Lim, L. Hooi, M. Rashid, E.K. Chow, Targeting Jak/Stat pathway as a therapeutic strategy against SP/CD44+ tumorigenic cells in Akt/β-catenin-driven hepatocellular carcinoma, J. Hepatol. 72 (1) (2020) 104–118.
[19] G.C. Jayson, R. Kerbel, L.M. Ellis, A.L. Harris, Antiangiogenic therapy in oncology: current status and future directions, Lancet 388 (10043) (2016) 518–529.
[20] H. Wu, T. Wang, Y. Liu, X. Li, S. Xu, C. Wu, H. Zou, M. Cao, G. Jin, J. Lang, B. Wang, B. Liu, X. Luo, C. Xu, Mitophagy promotes sorafenib resistance through hypoxia-inducible ATAD3A dependent Axis, J. Exp. Clin. Cancer Res. 39 (1) (2020) 274.
[21] W. Tang, Z. Chen, W. Zhang, Y. Cheng, B. Zhang, F. Wu, Q. Wang, S. Wang, D. Rong, F.P. Reiter, E.N. De Toni, X. Wang, The mechanisms of sorafenib resistance in hepatocellular carcinoma: theoretical basis and therapeutic aspects, Signal Transduct. Targeted Ther. 5 (1) (2020) 87.
[22] C. Méndez-Blanco, F. Fondevila, A. García-Palomo, J. González-Gallego, J. L. Mauriz, Sorafenib resistance in hepatocarcinoma: role of hypoxia-inducible factors, Exp. Mol. Med. 50 (10) (2018) 1–9.
[23] H. Lin, C. Yang, Y. Luo, M. Ge, H. Shen, X.L. Zhang, J.L. Shi, Biomimetic nanomedicine-triggered *in situ* vaccination for innate and adaptive immunity activations for bacterial osteomyelitis treatment, ACS Nano 16 (4) (2022) 5943–5960.
[24] A. Ulldemolins, J. Seras-Franzoso, F. Andrade, D. Rafael, I. Abasolo, P. Gener, S. Schwartz Jr., Perspectives of nano-carrier drug delivery systems to overcome cancer drug resistance in the clinics, Cancer Drug Resist 4 (1) (2021) 44–68.
[25] N. Yang, C. Cao, X. Lv, T. Zhang, J. Shao, X. Song, W. Wang, P. Chen, W. Huang, X. Dong, Photo-facilitated chemodynamic therapeutic agents: synthesis, mechanisms, and biomedical applications, BMEMat 1 (1) (2023), e12005.
[26] S. Guo, K. Li, B. Hu, C. Li, M. Zhang, A. Hussain, X. Wang, Q. Cheng, F. Yang, K. Ge, J. Zhang, J. Chang, X.J. Liang, Y. Weng, Y. Huang, Membrane-destabilizing ionizable lipid empowered imaging-guided siRNA delivery and cancer treatment, Exploration (Beijing) 1 (1) (2021) 35–49.
[27] Y. Zhao, Z. Zhang, Z. Pan, Y. Liu, Advanced bioactive nanomaterials for biomedical applications, Exploration (Beijing, China) 1 (3) (2021), 20210089.
[28] Y. Cai, Z. Wei, C. Song, C. Tang, W. Han, X. Dong, Optical nano-agents in the second near-infrared window for biomedical applications, Chem. Soc. Rev. 48 (1) (2019) 22–37.
[29] D. Chen, Z. Zhong, Q. Ma, J. Shao, W. Huang, X. Dong, Aza-BODIPY-based nanomedicines in cancer phototheranostics, ACS Appl. Mater. Interfaces 12 (24) (2020) 26914–26925.
[30] N. Yang, W. Xiao, X. Song, W. Wang, X. Dong, Recent advances in tumor microenvironment hydrogen peroxide-responsive materials for cancer photodynamic therapy, Nano-Micro Lett. 12 (1) (2020) 15.
[31] M. Ge, H. Guo, M. Zong, Z. Chen, Z. Liu, H. Lin, J. Shi, Bandgap-engineered germanene nanosheets as an efficient photodynamic agent for cancer therapy, Angew. Chem. Int. Ed. 62 (12) (2023), e202215795.
[32] Z. Wei, P. Liang, J. Xie, C. Song, C. Tang, Y. Wang, X. Yin, Y. Cai, W. Han, X. Dong, Carrier-free nano-integrated strategy for synergetic cancer anti-angiogenic therapy and phototherapy, Chem. Sci. 10 (9) (2019) 2778–2784.
[33] P. Liang, B. Ballou, X. Lv, W. Si, M.P. Bruchez, W. Huang, X. Dong, Monotherapy and combination therapy using anti-angiogenic nanoagents to fight cancer, Adv. Mater. 33 (15) (2021), e2005155.
[34] J. Zhu, X. Wang, Y. Su, J. Shao, X. Song, W. Wang, L. Zhong, L. Gan, Y. Zhao, X. Dong, Multifunctional Nanolocks with GSH as the Key for Synergistic Ferroptosis and Anti-chemotherapeutic Resistance, Biomaterials, 2022, 121704.
[35] Z. Li, Imaging of hydrogen peroxide (H(2)O(2)) during the ferroptosis process in living cancer cells with a practical fluorescence probe, Talanta 212 (2020), 120804.
[36] I. Vitale, G. Manic, L.M. Coussens, G. Kroemer, L. Galluzzi, Macrophages and metabolism in the tumor microenvironment, Cell Metabol. 30 (1) (2019) 36–50.
[37] Q. Tang, Z. Cheng, N. Yang, Q. Li, P. Wang, D. Chen, W. Wang, X. Song, X. Dong, Hydrangea-structured tumor microenvironment responsive degradable

nanoplatform for hypoxic tumor multimodal imaging and therapy, Biomaterials 205 (2019) 1–10.
[38] G. Yang, L. Xu, Y. Chao, J. Xu, X. Sun, Y. Wu, R. Peng, Z. Liu, Hollow MnO(2) as a tumor-microenvironment-responsive biodegradable nano-platform for combination therapy favoring antitumor immune responses, Nat. Commun. 8 (1) (2017) 902.
[39] B. Ding, P. Zheng, P. Ma, J. Lin, Manganese oxide nanomaterials: synthesis, properties, and theranostic applications, Adv. Mater. 32 (10) (2020), e1905823.
[40] W. Xu, X. Qing, S. Liu, Z. Chen, Y. Zhang, Manganese oxide nanomaterials for bacterial infection detection and therapy, J. Mater. Chem. B 10 (9) (2022) 1343–1358.
[41] Y. Miao, Y. Qiu, M. Zhang, K. Yan, P. Zhang, S. Lu, Z. Liu, X. Shi, X. Zhao, Aqueous self-assembly of block copolymers to form manganese oxide-based polymeric vesicles for tumor microenvironment-activated drug delivery, Nano-Micro Lett. 12 (1) (2020) 124.
[42] C. Liang, X. Zhang, Z. Wang, W. Wang, M. Yang, X. Dong, Organic/inorganic nanohybrids rejuvenate photodynamic cancer therapy, J. Mater. Chem. B 8 (22) (2020) 4748–4763.
[43] G. Yang, J. Ji, Z. Liu, Multifunctional MnO(2) nanoparticles for tumor microenvironment modulation and cancer therapy, Wiley Interdiscipl. Rev. Nanomed. Nanobiotechnol. 13 (6) (2021), e1720.
[44] P. Zhu, Y. Chen, J. Shi, Nanoenzyme-augmented cancer sonodynamic therapy by catalytic tumor oxygenation, ACS Nano 12 (4) (2018) 3780–3795.
[45] K. Xu, Z. Zhao, J. Zhang, W. Xue, H. Tong, H. Liu, W. Zhang, Albumin-stabilized manganese-based nanocomposites with sensitive tumor microenvironment responsivity and their application for efficient SiRNA delivery in brain tumors, J. Mater. Chem. B 8 (7) (2020) 1507–1515.
[46] W. Cheng, C. Liang, L. Xu, G. Liu, N. Gao, W. Tao, L. Luo, Y. Zuo, X. Wang, X. Zhang, X. Zeng, L. Mei, TPGS-functionalized polydopamine-modified mesoporous silica as drug nanocarriers for enhanced lung cancer chemotherapy against multidrug resistance, Small 13 (29) (2017).
[47] W. Cheng, J.P. Nie, N.S. Gao, G. Liu, W. Tao, X.J. Xiao, L.J. Jiang, Z.G. Liu, X. W. Zeng, L. Mei, A multifunctional nanoplatform against multidrug resistant cancer: merging the best of targeted chemo/gene/photothermal therapy, Adv. Funct. Mater. 27 (45) (2017).
[48] Y. Xia, Z. Xiao, X. Dou, H. Huang, X. Lu, R. Yan, Y. Gan, W. Zhu, J. Tu, W. Zhang, X. Tao, Green and facile fabrication of hollow porous MnO/C microspheres from microalgaes for lithium-ion batteries, ACS Nano 7 (8) (2013) 7083–7092.
[49] F. Gao, Y. Tang, W.L. Liu, M.Z. Zou, C. Huang, C.J. Liu, X.Z. Zhang, Intra/extracellular lactic acid exhaustion for synergistic metabolic therapy and immunotherapy of tumors, Adv. Mater. 31 (51) (2019), e1904639.
[50] L. Bejarano, M.J.C. Jordão, J.A. Joyce, Therapeutic targeting of the tumor microenvironment, Cancer Discov. 11 (4) (2021) 933–959.
[51] Y. Dai, C. Xu, X. Sun, X. Chen, Nanoparticle design strategies for enhanced anticancer therapy by exploiting the tumour microenvironment, Chem. Soc. Rev. 46 (12) (2017) 3830–3852.
[52] Z. Liu, S. Zhang, H. Lin, M. Zhao, H. Yao, L. Zhang, W. Peng, Y. Chen, Theranostic 2D ultrathin MnO(2) nanosheets with fast responsibility to endogenous tumor microenvironment and exogenous NIR irradiation, Biomaterials 155 (2018) 54–63.
[53] A. Jin, Y. Wang, K. Lin, L. Jiang, Nanoparticles modified by polydopamine: working as "drug" carriers, Bioact. Mater. 5 (3) (2020) 522–541.
[54] B. Cucarull, A. Tutusaus, T. Hernáez-Alsina, P. García de Frutos, M. Reig, A. Colell, M. Marí, A. Morales, Antioxidants threaten multikinase inhibitor efficacy against liver cancer by blocking mitochondrial reactive oxygen species, Antioxidants 10 (9) (2021).
[55] H. Li, Y. Yu, Y. Liu, Z. Luo, B.Y.K. Law, Y. Zheng, X. Huang, W. Li, Ursolic acid enhances the antitumor effects of sorafenib associated with Mcl-1-related apoptosis and SLC7A11-dependent ferroptosis in human cancer, Pharmacol. Res. 182 (2022), 106306.
[56] T. Kurosu, M. Ohki, N. Wu, H. Kagechika, O. Miura, Sorafenib induces apoptosis specifically in cells expressing BCR/ABL by inhibiting its kinase activity to activate the intrinsic mitochondrial pathway, Cancer Res. 69 (9) (2009) 3927–3936.
[57] Y.J. Zhu, B. Zheng, H.Y. Wang, L. Chen, New knowledge of the mechanisms of sorafenib resistance in liver cancer, Acta Pharmacol. Sin. 38 (5) (2017) 614–622.
[58] G. Powis, L. Kirkpatrick, Hypoxia inducible factor-1α as a cancer drug target, Mol. Cancer Therapeut. 3 (5) (2004) 647–654.
[59] C. Mendez-Blanco, F. Fondevila, A. Garcia-Palomo, J. Gonzalez-Gallego, J. L. Mauriz, Sorafenib resistance in hepatocarcinoma: role of hypoxia-inducible factors, Exp. Mol. Med. 50 (2018).
[60] Y. Liang, T. Zheng, R. Song, J. Wang, D. Yin, L. Wang, H. Liu, L. Tian, X. Fang, X. Meng, H. Jiang, J. Liu, L. Liu, Hypoxia-mediated sorafenib resistance can be overcome by EF24 through Von Hippel-Lindau tumor suppressor-dependent HIF-1α inhibition in hepatocellular carcinoma, Hepatology 57 (5) (2013) 1847–1857.
[61] Y. Wan, L.H. Fu, C. Li, J. Lin, P. Huang, Conquering the hypoxia limitation for photodynamic therapy, Adv. Mater. 33 (48) (2021), e2103978.
[62] M.H. Bao, C.C. Wong, Hypoxia, metabolic reprogramming, and drug resistance in liver cancer, Cells 10 (7) (2021).
[63] W.J. Xu, X. Qing, S.L. Liu, D.L. Yang, X.C. Dong, Y.W. Zhang, Hollow mesoporous manganese oxides: application in cancer diagnosis and therapy, Small 18 (15) (2022).
[64] M. Shu, J. Tang, L. Chen, Q. Zeng, C. Li, S. Xiao, Z. Jiang, J. Liu, Tumor microenvironment triple-responsive nanoparticles enable enhanced tumor penetration and synergetic chemo-photodynamic therapy, Biomaterials 268 (2021), 120574.